Draft version December 2, 2020
Typeset using LaTeX **twocolumn** style in AASTeX62

Galaxy Lookback Evolution Models - a Comparison with Magneticum Cosmological Simulations and Observations

Rolf-Peter Kudritzki,[1,2] Adelheid F. Teklu,[1,3] Felix Schulze,[1,4] Rhea-Silvia Remus,[1] Klaus Dolag,[1,5] Andreas Burkert,[1,4] and H. Jabran Zahid[6]

[1] *LMU München, Universitätssternwarte, Scheinerstr. 1, 81679 München, Germany*
[2] *Institute for Astronomy, University of Hawaii at Manoa, 2680 Woodlawn Drive, Honolulu, HI 96822, USA*
[3] *Excellence Cluster Origins, Boltzmannstr. 2, 85748 Garching, Germany*
[4] *Max Planck Institute for Extraterrestrial Physics, Giessenbachstr. 1, 85748 Garching, Germany*
[5] *Max Planck Institute for Astrophysics, Karl-Schwarzschildstr. 1, 85748 Garching, Germany*
[6] *Microsoft Research, 14820 NE 36th St, Redmond, WA 98052, USA*

Submitted to ApJ

ABSTRACT

We construct empirical models of star-forming galaxy evolution assuming that individual galaxies evolve along well-known scaling relations between stellar mass, gas mass and star formation rate following a simple description of chemical evolution. We test these models by a comparison with observations and with detailed Magneticum high resolution hydrodynamic cosmological simulations. Galaxy star formation rates, stellar masses, gas masses, ages, interstellar medium and stellar metallicities are compared. It is found that these simple lookback models capture many of the crucial aspects of galaxy evolution reasonably well. Their key assumption of a redshift dependent power law relationship between galaxy interstellar medium gas mass and stellar mass is in agreement with the outcome of the complex Magneticum simulations. Star formation rates decline towards lower redshift not because galaxies are running out of gas, but because the fraction of the cold ISM gas, which is capable of producing stars, becomes significantly smaller. Gas accretion rates in both model approaches are of the same order of magnitude. Metallicity in the Magneticum simulations increases with ratio of stellar mass to gas mass as predicted by the lookback models. The mass metallicity relationships agree and the star formation rate dependence of these relationships is also reproduced. We conclude that these simple models provide a powerful tool for constraining and interpreting more complex models based on cosmological simulations and for population synthesis studies analyzing integrated spectra of stellar populations.

Keywords: galaxies: evolution, metallicity, gas masses, accretion, star formation

1. INTRODUCTION

Observations of galaxies through cosmic time and detailed hydrodynamic cosmological simulations show that the formation and evolution of galaxies is an extremely complicated process. At high redshifts, the first building blocks of galaxies contract and form the first stars while gas continues to accrete from the intergalactic medium, providing new additional fuel for star formation. At the same time stars produce heavy elements (metals) through the nuclear fusion processes in their interior. Some of the newly produced metals together with some hydrogen and helium are recycled to the interstellar medium (ISM) by a variety of complex stellar mass-loss processes. While stars continue to form and gas is continuously accreted, metals accumulate during the life of a galaxy, but at the same time a significant fraction of the metals appears to be expelled from the ISM by large scale galactic winds. In addition, merging processes with infalling other nearby galaxies influence the evolution significantly.

Corresponding author: Rolf-Peter Kudritzki
kud@ifa.hawaii.edu

In view of the complexity of these many processes and their interplay on different time scales it is surprising that an intriguingly simple relationship exists between total galactic stellar mass and the average metallicity of galaxies, the mass-metallicity relationship ("MZR"), see for example Lequeux et al. (1979), Tremonti et al. (2004), Kudritzki et al. (2016)(herafter K16), Zahid et al. (2017) (herafter Z17). This MZR and its evolution with redshift appears like a true Rosetta stone to understand the key aspects of galaxy evolution. For instance, Zahid et al. (2014) (hereafter Z14) show that the observed MZRs at different redshift can be explained by a very simple model with galactic winds and accretion where the observed metallicity is a function of the ratio of galactic stellar to ISM gas mass. Over their lifetime star forming galaxies evolve along the (redshift dependent) main sequence of star formation and turn gas into stars. During this evolution the low-mass metal-poor galaxies are gas-rich and the high-mass metal-rich galaxies are gas-poor (see Fig. 5 and 7 in Z14).

Given the success of the Z14 approach in matching and explaining the observations it appears important to further investigate the validity of this rather simple galaxy evolution model. An obvious way is the comparison with cosmological simulations, which describe the complicated processes during the formation and evolution of galaxies in a much more comprehensive way. This is done in the following by using the extensive Magneticum simulations (see section 4).

Starting from the ideas described in Z14 and Z17 we develop a new generation of lookback models, which describe the evolution of galaxies. We then compare the properties of these models (SFR ψ, stellar mass M_*, ISM gas mass M_g, luminosity weighted age t of the stellar population and logarithmic metallicity [Z] of the ISM and the stellar population) with the properties of galaxies in the Magneticum Box 4 (high resolution) simulations. We also compare with observations.

2. LOOKBACK MODELS

Our goal is to describe the evolution of a galaxy, which is observed at a redshift z_0 with a stellar mass $M^*(z_0)$ back to its origin. Because we are looking back in cosmic time, we call these models lookback models. The relationship between lookback time and redshift z is given by the standard equations

$$t(z) = t(z_0) + \frac{1}{H_0}\int_{z_0}^{z} \frac{dz}{(1+z)E(z)} \quad (1)$$

with E(z)

$$E(z) = (\Omega_\Lambda + \Omega_m(1+z)^3)^{\frac{1}{2}} \quad (2)$$

and

$$t(z_0) = \frac{1}{H_0}\int_{0}^{z_0} \frac{dz}{(1+z)E(z)}. \quad (3)$$

Like the Magneticum simulations (see section 4) we adopt a flat universe with $H_0 = 70.4$ km/sec/Mpc = 70.4×1.023^{-12}yr^{-1} and densities $\Omega_\Lambda = 0.728$ and Ω_m = 1 - Ω_Λ.

The mass evolution is then described by

$$M_*(z) = M_*(z_0) - \frac{(1-R)}{H_0}\int_{z_0}^{z} \frac{\psi(M_*,z)}{(1+z)E(z)}dz. \quad (4)$$

R is the fraction of stellar mass which is returned to the interstellar medium because of stellar winds and supernova explosions. Following Z14 and Z17 we adopt R = 0.45 based on the assumption of a Chabrier (2003) stellar initial mass function. ψ is the star formation rate (SFR) as a function of stellar mass and redshift. We use a modified form (see section 5 below) of the SFR law from Pearson et al. (2018), Appendix C, which is based on observations of galaxies on the star foming main sequences out to redshift z = 6. We usually finish the integration, when a minimum stellar mass of 10^6 $M_\odot$ is reached.

A key simplification in our approach is the assumption that at every redshift there is a power law correlation between the total mass of the cold (molecular and atomic) gas of the ISM and the stellar mass of galaxies

$$M_g(z) = A(z)M_*^\beta(z) \quad (5)$$

with

$$A(z) = A_0(1+z)^\alpha. \quad (6)$$

This assumption is based on survey observations of star forming galaxies in the local Universe, which indicate a power law holding over several orders of magnitude in stellar mass with an exponent of the order of $\beta \sim 0.5$ (see Z14, Peeples et al. 2014, Saintonge et al. 2017, Catinella et al. 2018, Hunt et al. 2020). The redshift dependence was introduced by Z14 to match the observed ISM oxygen abundance MZRs out to higher redshift. We will use the same procedure for our new models and give new values for α, β and A_0 below.

The chemical evolution is described by the metallicity equation for the metallicity mass fraction Z (for all details see Z14)

$$\frac{dZ}{dM_*} = \frac{1}{M_g}(\frac{dM_Z}{dM_*} - Z\frac{dM_g}{dM_*}), \quad (7)$$

where the change of the metallicity mass M_Z of the ISM is given by

$$\frac{dM_z}{dM_*} = Y_N - Z(1-R). \tag{8}$$

Y_N is the effective yield, which in addition to the stellar nucleosynthesis yield Y includes the effects of accretion from the halo and the intergalactic medium (dM_{accr}) and galactic winds (dM_{wind}) as described by Z14

$$Y_N = Y - \zeta \tag{9}$$

with

$$\zeta = Z_{wind}\frac{dM_{wind}}{dM_*} - Z_{accr}\frac{dM_{accr}}{dM_*}. \tag{10}$$

Z_{accr} is the metallicity of the accreted gas, while Z_{wind} corresponds to the metallicity of the matter lost through galactic winds. Based on observational evidence provided by Zahid et al. (2012) and Peeples et al. (2014), Z14 argue convincingly that $\zeta\sim$ const. is a reasonable approximation. We therefore use $Y_N \sim$ const. as a free parameter noting that it consists of two components, the nucleosynthesis yield Y and the effects of accretion and winds described by ζ.

Using eq. (5) and (6) we can express $\frac{dM_g}{dM_*}$ as

$$\frac{dM_g}{dM_*} = \beta\frac{M_g}{M_*}(1 - K(M_*, z)) \tag{11}$$

with

$$K(M_*, z) = \frac{\alpha}{\beta}H_0\frac{E(z)}{(1-R)\psi}M_*. \tag{12}$$

The function K describes the influence of the evolution with redshift of the power law relation between stellar mass and gas mass.

Eq. (11) then leads to the final form of the metallicity equation

$$\frac{dZ}{dM_*} = \frac{1-R}{M_g}\{\frac{Y_N}{1-R} - Z\left(1 + \frac{\beta}{1-R}\frac{M_g}{M_*}(1-K)\right)\}. \tag{13}$$

We note that Z14 in their analytical approach neglect the second term on the right hand side of eq. (7). However, solving our set of lookback model equations numerically and calculating a large grid of models with different model parameters we find that including this term leads to a small, but non-negligible quantitative difference in the calculated metallicity during the evolution of a galaxy. We, therefore, keep this term for the calculation of our numerical lookback models and develop a new analytical solution later in Appendix A.

Fig. 1 shows a typical result for the lookback model evolution of seven galaxies with different final masses (a yield of $\log\frac{Y_N}{Z_\odot(1-R)} = 0.3$ and the star formation law

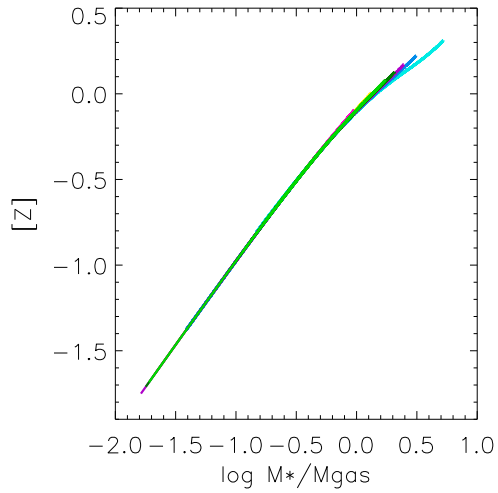

Figure 1. Lookback model ISM metallicity [Z] as a function of the ratio of stellar mass to gas mass for the evolution of 7 galaxies with final masses of log M_* = 9.28, 9.65, 10.01, 10.16, 10.34, 10.60, 11.13. We use different colors for the galaxy evolution tracks with different final mass. Note that the tracks lie on top of each other, which means that [Z] depends only on M_*/M_g. For the defintion of [Z] see equation (14). The result is discussed in detail in Appendix A and the calculations are described in section 2.

described in section 5 have been used for these calculations). While there is a small quantitative difference to the Z14 results, we see that the most important property of the lookback models remains. Metallicity is to a good approximation solely a function of the ratio of stellar mass to gas mass M_*/M_g. As we show in Appendix A, this is the consequence of the key assumption of our lookback models, the relationship between gas mass and stellar mass as described by eq. (5) and (6). The comparison with the Magneticum models will be an important check whether this key assumption is valid.

In the following we will express metallicities in units of the solar metallicity defined as

$$[Z] = \log Z/Z_\odot. \tag{14}$$

For the metallicity mass fraction of the sun we will use $Z_\odot = 0.014$ (Asplund et al. 2009).

The metallicity shown in Fig. 1 is the metallicity of the ISM and the stars just born from this ISM. For the comparison with stellar metallicities we will also calculate a V-band luminosity weighted average over the whole galactic population of stars, which includes all stars that formed earlier at lower metallicity. For this calculation we adopt the Chabrier (2003) stellar initial mass function.

3. OBSERVATIONS

To compare our model calculations with observations we use galaxy metallicities derived from quantitative stellar spectroscopy of individual blue and red supergiant stars in nearby galaxies out to 20 Mpc (see K16) and population synthesis stellar spectroscopy of stacked spectra of 250000 SDSS galaxies at a redshift of z $\sim$ 0.08 (see Z17). We also include observational results obtained from HII region strong line studies at z = 0.08, 0.29, 0.78, 1.55, 2.3 and 3.3 from Sanders et al. (2020) (violet circles: their Table 1; yellow circles: eq. 10 with SFR from eq. 2, 3, 4), Genzel et al. (2015) (their eq. 12a) and Z14 (their Table 2 and eq. 5). The Z14 strong line oxygen abundances were based on the Kobulnicky & Kewley (2004) calibration. According to the work by K16 and Bresolin et al. (2016) the N2 calibration by Pettini & Pagel (2004) is more appropriate. We have therefore transformed the Z14 abundances to this calibration using the transformation suggested by Kewley & Ellison (2008). The Genzel et al. (2015) and Sanders et al. (2020) oxygen abundances were already determined using the Pettini & Pagel (2004) calibration and do not require a transformation adjustment.

Fig. 2 shows the comparison of our lookback models with the observations. The calculations use the parameters $\alpha = 0.40$, $\beta = 0.60$, log $A_0 = 3.73$ (see eq. 5 and 6, M_* and M_g in solar masses) and $\log \frac{Y_N}{Z_\odot(1-R)} = 0.225$ and apply a main sequence star formation law as described in section 5 with the correction factor c(z) set to unity. We find remarkable agreement.

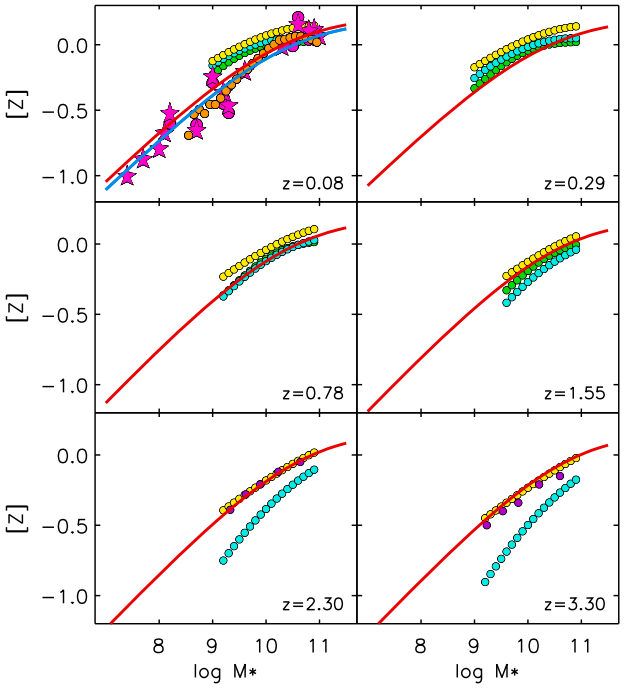

Figure 2. Lookback model MZRs at different redshifts. The metallicity of the ISM and the young stellar population versus the total stellar mass of the galaxy is shown in red. The blue curve represents the V-band luminosity weighted metallicity of the whole stellar population. Observed HII-region MZRs at the same redshift are shown in green (Zahid et al. 2014), cyan (Genzel et al. 2015), yellow and violet (Sanders et al. 2020). For the lowest redshift we also show observations of the stellar metallicities of the young stellar population (pink circles: red supergiant stars; pink stars: blue supergiant stars, see Kudritzki et al. 2016). The orange circles respresent metallicities of the young stellar population obtained by population synthesis analysis of SDSS spectra of the integrated stellar population of a large sample of galaxies (Zahid et al. 2017).

4. MAGNETICUM DATA

The Magneticum[1] simulations are a set of fully hydrodynamical cosmological simulations of different box-volumes and resolutions. They follow the formation and evolution of cosmological structures through cosmic time, accounting for the complex physical processes which shape the first building blocks of galaxies into the mature galaxies of today. For details on these simulations see Hirschmann et al. (2014) and Teklu et al. (2015). A WMAP-7 ΛCDM cosmology (Komatsu et al. 2011) is adopted with $h = 0.704$, $\Omega_m = 0.272$, $\Omega_b = 0.0451$, $\Omega_\lambda = 0.728$, $\sigma_8 = 0.809$, and an initial slope of the power spectrum of $n_s = 0.963$.

Specifically, as this is relevant to the work presented here, metal radiative cooling is implemented according to Wiersma et al. (2009), i.e. the interstellar medium is treated as a two-phase medium where clouds of cold gas are embedded in the hot gas phase. Star formation and galactic winds are treated in the same way as described by Springel & Hernquist (2003). Metals and energy are released by stars of different mass by integrating the evolution of the stellar population (for details see Dolag et al. 2017), properly accounting for mass-dependent lifetimes using a lifetime function according to Padovani & Matteucci (1993), the metallicity-dependent stellar yields by Woosley & Weaver (1995) for SNe II, the yields by van den Hoek & Groenewegen (1997) for AGB stars, and the yields by Thielemann et al. (2003) for SNeIa. Stars of different mass are initially distributed according to a Chabrier initial mass function Chabrier (2003).

For our comparison with the model calculations and observations we use the Magneticum Box 4 uhr simula-

[1] www.magneticum.org

tion. This simulation has a Box volume of (48 Mpc/h)^3 with initially 2x5763 (dark matter and gas) particles. The particle masses are $m_{\rm DM} = 3.6 \times 10^7 M_\odot$/h and $m_{\rm Gas} = 7.3 \times 10^6 M_\odot$/h, respectively, and each gas particle can spawn up to four stellar particles (i.e. the stellar particle mass is approximately 1/4th of the gas particle mass), with a softening of $\epsilon_{\rm DM} = \epsilon_{\rm Gas} = 1.4$ kpc/h and $\epsilon_* = 0.7$ kpc/h.

From this simulation we use two data sets: The first one is a snapshot of star forming galaxies at different redshifts, z $\sim$ 0.1 (exact 0.07), $\sim$ 0.5 (0.47), $\sim$ 1.0 (0.99), $\sim$ 1.5 (1.48), $\sim$ 2.0 (1.98), $\sim$ 2.8 (2.79), $\sim$ 3.4 (3.42), $\sim$ 4.2 (4.23), $\sim$ 5.3 (5.34), $\sim$ 6.9 (6.94). The second data set combines galaxies in stellar mass bins at redshift z = 0.07 and traces their evolution back in time at each time (or redshift) calculating averaged properties of the sample. The mass bins are log M$_*$ = 9.28, 9.65, 10.01, 10.16, 10.34, 10.60, 11.31 and the evolution is traced up to redshift z = 4.2. The selected mass bins are an arbirary choice to represent the range from lower to higher galaxy stellar masses. We call the first data set the redshift "snap shot sample" and the second one the "evolution sample". In the snap shot sample we distinguish between disk galaxies and intermediate galaxies. For this we use the position of a galaxy in the stellar mass–angular momentum plane, quantified by the b-value

$$b = \log(\frac{j}{\text{kpc km/s}}) - \frac{2}{3}\log(\frac{M_*}{M_\odot}), \qquad (15)$$

where j is the specific angular momentum of the galaxy stellar component (see especially Teklu et al. 2017, but also Teklu et al. 2015 and Schulze et al. 2018 for more details). At redshift z = 0.07, galaxies with -4.35 $\geq$ b $\geq$ -4.75 are classified as intermediates, whereas galaxies with b $\geq$ -4.35 are considered disks. Note that intermediates are a transitional galaxy type between disks and spheroids.

For the evolution sample we select all disk galaxies at z = 0.07 with log M$_*$ $\geq$ 9. Note that at higher redshift these galaxies could also have been intermediates or spheroids.

5. STAR FORMATION RATES

For the comparison with the Magneticum simulations we need to adopt a SFR law ψ(M$_*$,z), which provides SFRs as a function of stellar mass and redshift. There is a rich literature of observed SFR laws of the so-called galaxy main sequences (see, for instance, Pearson et al. 2018, Tacconi et al. 2020 for a recent summary). Most of the approaches describe star formation as a power law

$$\psi(z, M_*) = \psi_0(z) M_*^{\delta(z)}, \qquad (16)$$

where both the zero point $\psi_0(z)$ and the slope $\delta(z)$ increase with redshift. ψ is given in solar masses per year and the stellar masses are in solar units. We have selected a few published SFR laws (Elbaz et al. 2007, Behroozi et al. 2013, Speagle et al. 2014, Schreiber et al. 2015, Pearson et al. 2018, Sanders et al. 2020) and compare them with the Magneticum SFRs in Fig. 3. Given the systematic uncertainties of the observations (see the example discussed below) the comparison is reasonable and indicates that the sub-grid physics treatment of star formation adapted from Springel & Hernquist (2003) works well. However, we note a systematic difference at low and intermediate redshifts where the Magneticum SFRs are lower by a factor of 2 to 3.

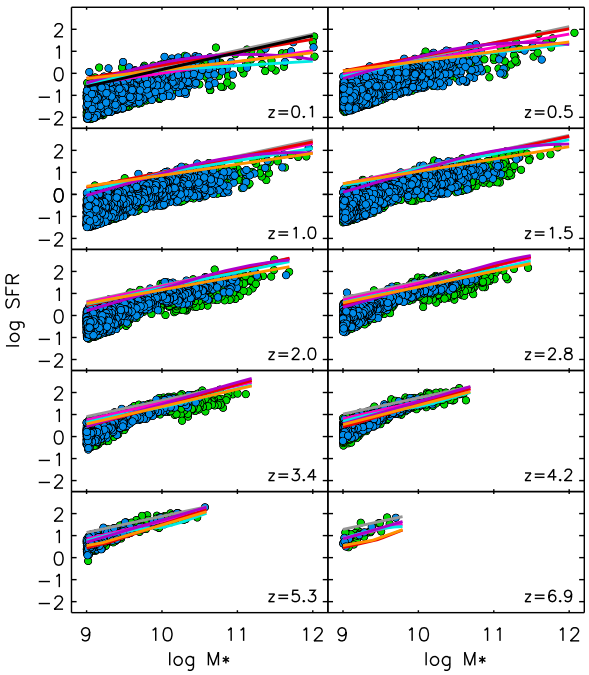

Figure 3. Logarithm of star formation rates of the Magneticum snap shot samples at different redshifts as a function of the logarithm of stellar mass (green circles: intermediates, blue circles: disks). Observed star formation rates are overplotted as solid curves: black: Elbaz et al. (2007), cyan: Behroozi et al. (2013), violet: Schreiber et al. (2015), orange: Pearson et al. (2018), red: Pearson et al. (2018), Appendix C, pink: Speagle et al. (2014), grey: Sanders et al. (2020).

In principle, we can construct lookback models with any reasonable star formation main sequence representation. For instance, for the comparison with observations in Fig. 2 we have used Pearson et al. (2018) as described in their Appendix C. However, the purpose of this work is to compare our simple lookback model approach with the highly complex and detailed hydrodynamic Mag-

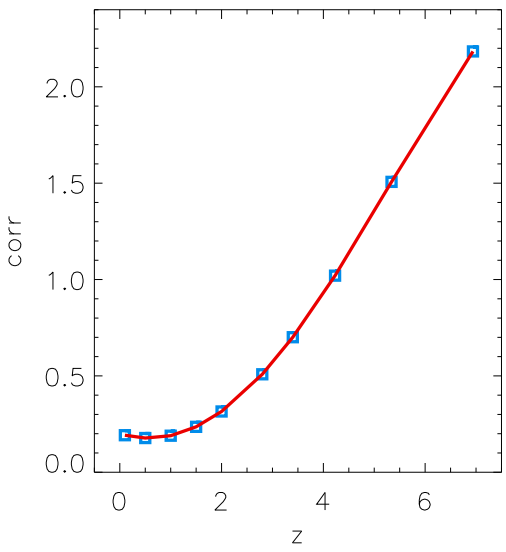

Figure 4. Correction factor applied to the Pearson et al. (2018) star formation rates as a function of redshift to match the Magneticum SFRs (see text).

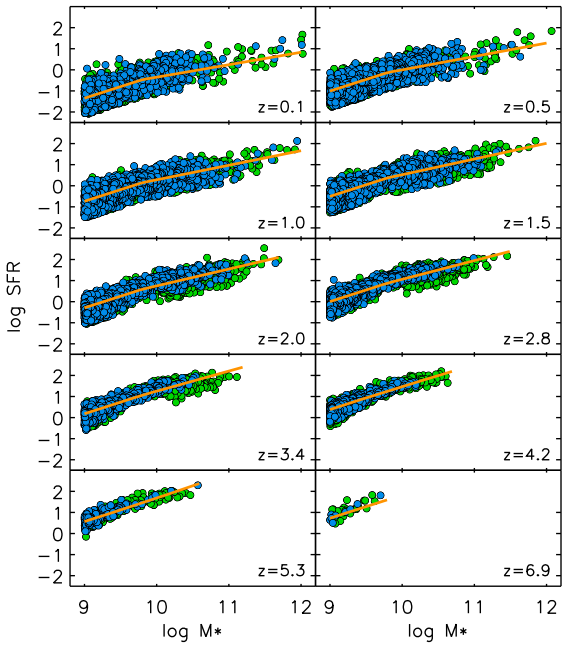

Figure 5. Same as Fig. 3 but now with the adopted lookback model star formation rates overplotted in orange (see text).

neticum simulations. Therefore, it is prudent to adopt a SFR description which matches the Magneticum SFRs reasonably well. We accomplish this by again using the Pearson et al. (2018) SFR law of their Appendix C, however now with several modifications. Most importantly, we apply a redshift dependent correction factor c(z) to $\psi_0(z)$

$$\psi_0^{LB}(z) = \psi_0(z)c(z), \tag{17}$$

which is shown in Fig. 4. With this factor we obtain a star formation law $\psi_{LB}(z, M_*)$ which is in good agreement with the Magneticum SFRs at $M_* = 10^{10.5} M_\odot$. In addition, we introduce a broken power law with respect to stellar mass, which is described in more detail in Appendix B together with the complete description of $\psi_{LB}(z, M_*)$.

Fig. 5 shows that ψ_{LB} provides a good representation of the average SFRs of the Magneticum snap shot sample. While the literature main sequence SFRs shown in Fig. 3 indicate that our adopted Magneticum matching star formation law ψ_{LB} may underestimate the observed main sequence SFRs at lower and intermediate redshift, the comparison in Fig. 6 with observed SFRs obtained by the xGASS and xCOLDGASS surveys (Saintonge et al. 2017, Catinella et al. 2018) of nearby galaxies indicates good agreement. We also note that the MAGMA survey (see Hunt et al. 2020) agrees well with Magneticum and ψ_{LB} except at the very low mass end of log $M_* \approx 9$, where the MAGMA SFRs are 0.3 dex larger.

We can also compare the time evolution of the Magneticum evolution sample with the ψ_{LB} of our lookback models. This is done in Fig. 7, where specific SFRs (sSFR) ψ/M_* are plotted for models corresponding to different Magneticum evolution mass bins. We conclude that the Magneticum SFRs are well represented by our choice of ψ_{LB}.

We note that in the complete snap shot set of Magneticum simulations there is a significant number of disk and intermediate galaxies with very low SFRs. Since this work focusses on star forming galaxies not too far from the main sequences, we have excluded those objects in Fig. 3 and from all further comparison between lookback models and Magneticum. As a selection criterion we use the threshold of 0.8 dex below our adopted star formation law and include only galaxies above this threshold. We realize that such galaxies with low SFRs below our threshold may exist in the real universe, but would be excluded from samples selected on strength of ISM emission lines.

6. COMPARISON BETWEEN LOOKBACK MODELS AND MAGNETICUM SIMULATIONS

6.1. *The relationship between gas mass and stellar mass*

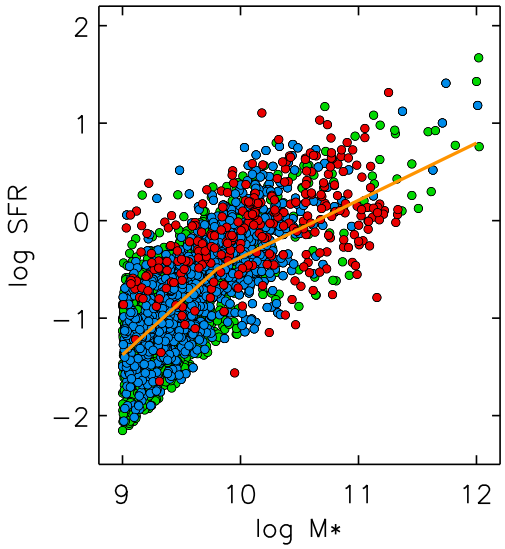

Figure 6. Magneticum snap shot star formation rates at redshift z = 0.1 (green and blue circles as before) compared with the observed star formation rates of the xGASS and xCOLDGASS surveys (red circles, for references see text). The adopted lookback model star formation rates are overplotted in orange.

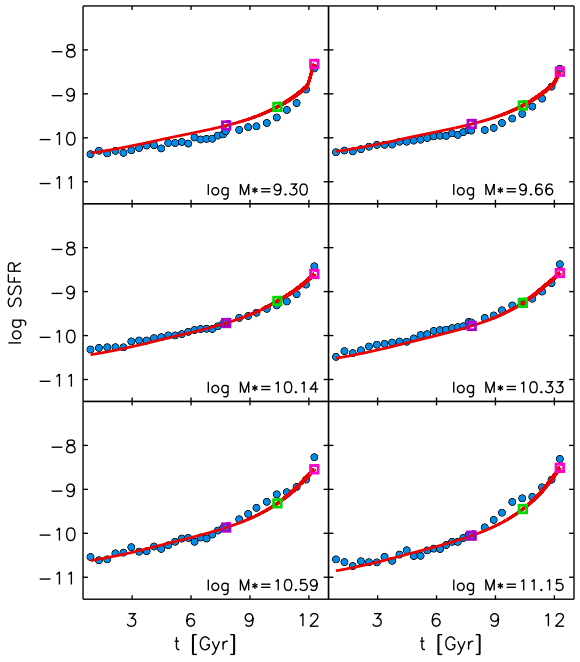

Figure 7. Specific star formation rate as a function of lookback time for six galaxies with different final stellar mass (at t = 0). The red curves correspond to lookback model calculations. The violet, green and pink squares indicate redshifts z = 1, 2 and 4.2, respectively. The blue circles correspond to the Magneticum evolution sample described in the text.

The key simplification of the lookback models is the assumption of a redshift dependent power law between galaxy stellar mass and the total mass of the cold ISM gas (see eq. 5 and 6). In Fig. 8 we test whether the Magneticum hydrodynamic cosmological simulations support the idea of such a relationship. We find good agreement with the Magneticum simulations. This result is very reassuring for the lookback model approach. It is a strong confirmation of the basic concept of these models. It also provides a substantial simplification for the description of star forming galaxy evolution.

One might argue that for galaxies on the main squence, where star formation follows a power law with stellar mass, it is to be expected that ISM gas mass depends on stellar mass in a similar way, because star formation should be proportional to gas mass. However, the situation is more complicated, because not all the ISM gas is involved in the star formation process and the fraction of star forming to total ISM gas changes with stellar mass and redshift. We will discuss this further below.

Nonetheless, we note that there is a weak star formation dependence of the relationship between ISM gas and stellar mass in the Magneticum snapshot sample. Galaxies with lower gas mass tend to have lower SFRs and higher gas mass galaxies have higher SFRs. This has consequences for the MZR and its SFR dependence, which will be discussed this further below.

6.2. *Luminosity weighted ages of the stellar population*

As the result of their different star formation histories the distribution of ages of the stellar populations in different galaxies will vary. A crucial quantity to characterize the age distribution is the luminosity weighted average age. In Fig. 9 we show the V-band luminosity weighted ages of the Magneticum galaxies as a function of stellar mass for different redshifts and compare with the lookback model predictions. Except for the lowest redshifts the lookback models seem to agree with the Magneticum simulations. However, we note a large spread of stellar ages for the Magneticum galaxies.

Since ages are related to star formation history, it is a crucial first test to investigate whether the age spread is correlated with SFRs. From Fig. 5 we know that our Magneticum snap shot sample has a wide range of SFRs ($\approx \pm$ 0.8 dex) at fixed stellar mass. We define five SFR bins for the Magneticum SFRs ψ_{Magn} with respect to the adopted lookback SFRs ψ_{LB} in the following way: bin1: log $\psi_{Magn}/\psi_{LB} \leq$ -0.5; bin2: -0.5 $\leq \psi_{Magn}/\psi_{LB} \leq$ -0.25; bin 3: -0.25 $\leq \psi_{Magn}/\psi_{LB} \leq$

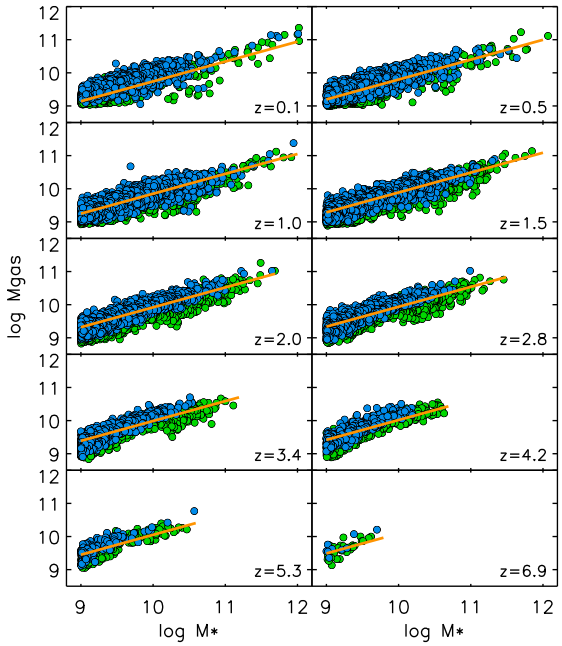

Figure 8. Logarithm of galaxy cold ISM gas mass versus logarithm of stellar mass at different redshifts. The Magneticum galaxies are shown as blue and green circles as before. The lookback model relationship is plotted as the orange line.

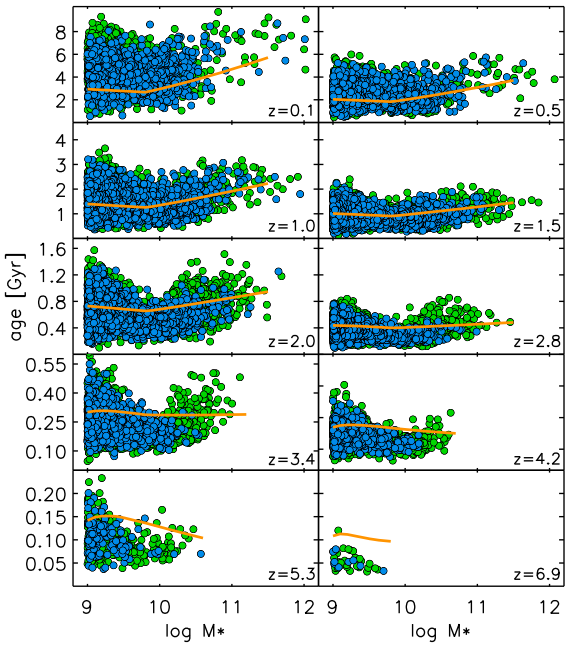

Figure 9. V-band luminosity weighted average ages (in Gyr) of the Magneticum galaxies stellar populations (green and blue circles as before) compared with ages calculated from the lookback models using the standard lookback model SFR law ψ_{LB} (orange) described in section 5.

+0.25; bin4: $+0.25 \leq \psi_{Magn}/\psi_{LB} \leq +0.50$; bin5: $+0.5 \leq \psi_{Magn}/\psi_{LB}$.

Fig. 10 shows the ages of the Magneticum galaxies again but now color coded with respect to SFR bin. There is an obvious anti-correlation between age and star formation rate, which is easy to understand. The oldest galaxies at a given stellar mass are mostly those with the lowest SFRs, because it took a long time to build up the stellar mass, and the youngest are mostly those with high SFRs, because the stellar mass was built up recently.

To simulate the effect of systematically higher and lower star formation rates we have also calculated lookback models with SFRs of log $\psi_{LB} \pm 0.375$. The luminosity weighted ages of the stellar population of these models are also shown in Fig. 10. We see that by accounting for systematically higher or lower SFRs in the lookback models we obtain ages in agreement with Magneticum.

6.3. *Gas accretion*

In the previous subsections we compared the lookback models with the Magneticum snap shot sample, the set of simulated star forming galaxies at different redshifts. Now we turn to the Magneticum evolution sample, where we combine galaxies in stellar mass bins and then follow their evolution with time calculating averaged properties of each mass bin as a function of time (or redshift). In a first step we study the evolution of galaxy gas mass and investigate the role of gas accretion. Both the lookback models and the Magneticum simulations include the effect of gas accretion from the galactic halo or the intergalactic medium. In the case of the lookback models this is done implicitly through the assumption of the power law relationship between gas and stellar mass $\mathrm{M}_g = \mathrm{A(z)M}_*^{\beta}$. In the case of the Magneticum models this is a direct result of the hydrodynamic simulation of the galaxy formation and evolution process. The change of gas mass with redshift (or time) is given by

$$\Delta M_g = \Delta M_{\mathrm{accr}}^{\mathrm{eff}} - \Delta M_* \tag{18}$$

where ΔM_* is the change of stellar mass through star formation, which causes a decrease of gas mass. $\Delta M_{\mathrm{accr}}^{\mathrm{eff}}$ is the net amount of accreted gas mass leading to an increase of ISM gas mass and consists of two terms

$$\Delta M_{\mathrm{accr}}^{\mathrm{eff}} = \Delta M_{\mathrm{accr}} - \Delta M_{\mathrm{wind}}, \tag{19}$$

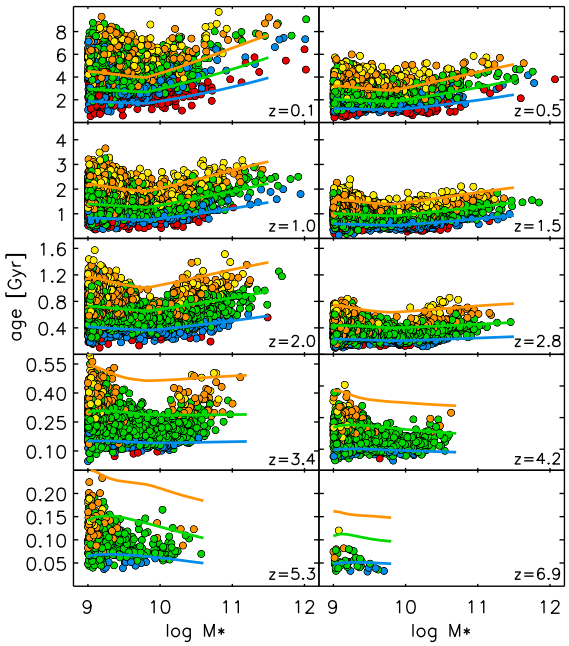

Figure 10. Same as Fig. 9 but now the Magneticum galaxies are color-coded with respect to SFR. Bin1: yellow, bin2: orange, bin3: green, bin4: blue, bin5: red. Bin 1 corresponds to the lowest SFRs and bin 5 to the highest (for the extact definition see text). The green curve corresponds to ages calculated with the standard lookback model SFR law ψ_{LB}. The orange and blue curves are obtained from lookback model calculations, where log ψ_{LB} is modified by offsets of -0.375 dex and +0.375 dex, respectively.

where the first describes mass gain through accretion and the second term mass loss through galactic winds. The normalized effective accretion rate $\Lambda_{\rm eff}$ is then

$$\Lambda_{\rm eff} = \frac{\Delta M^{\rm eff}_{\rm accr}}{\Delta M_*} = \frac{\Delta M_g}{\Delta M_*} + 1. \qquad (20)$$

We note that the normalized effective accretion rate is equal to the effective mass accretion factor, which is frequently used in chemical evolution models (see, for instance, Kudritzki et al. 2015)

$$\Lambda_{\rm eff} = \frac{\dot{M}_{\rm accr}}{(1-R)\psi} - \frac{\dot{M}_{\rm wind}}{(1-R)\psi}, \qquad (21)$$

where $\dot{M}_{\rm wind}$ and $\dot{M}_{\rm accr}$ are the rates of mass-loss through winds and mass-gain through accretion, respectively. In the case of the lookback models the normalized effective accretion rate can be calculated analytically (see section 2)

$$\Lambda_{\rm eff} = 1 + \beta \frac{M_g}{M_*}(1 - K(M_*, z)). \qquad (22)$$

Fig. 11 shows the accretion rates of the lookback models (red curves) as a function of time for the galaxies with six final masses log M_*. We see that accretion dominates over galactic winds ($\Lambda_{\rm eff} > 0$) but the mass gains through accretion rates are moderate and do not exceed the SFRs by a large factor. For the lookback models the value of $\Lambda_{\rm eff} \approx 1$ implies accretion rates half of the SFRs (note that 1 - R = 0.55 for the look back models). The $\Lambda_{\rm eff}$ rates of the Magneticum simulations are of the same order for the four higher galaxy masses, but are larger by a factor two to three for log $M_* = 9.30$ and 9.66, respectively.

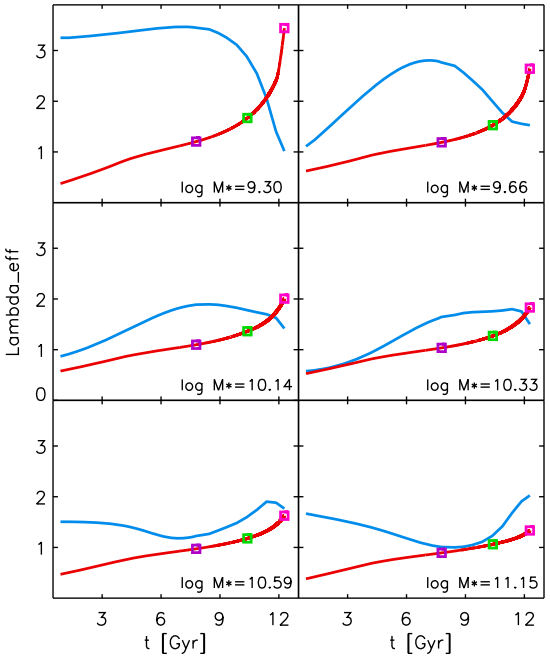

Figure 11. Normalized effective accretion rate as a function of lookback time for six galaxies with different final stellar mass (at t = 0). The red curves correspond to lookback model calculations. The violet, green and pink squares indicate redshifts z = 1, 2 and 4.2, respectively. The blue curves are calculated from the Magneticum evolution sample described in the text.

While the differences between the lookback models with the simple assumption of a redshift dependent power law relationship between gas mass and stellar mass and the detailed Magneticum hydrodynamic simulations are obvious, we note that they are not orders of magnitude. We take this as an additional confirmation of the lookback model approach. As we will see in the next subsection, this is mostly caused by somewhat higher values of R and not so much by higher accretion rates.

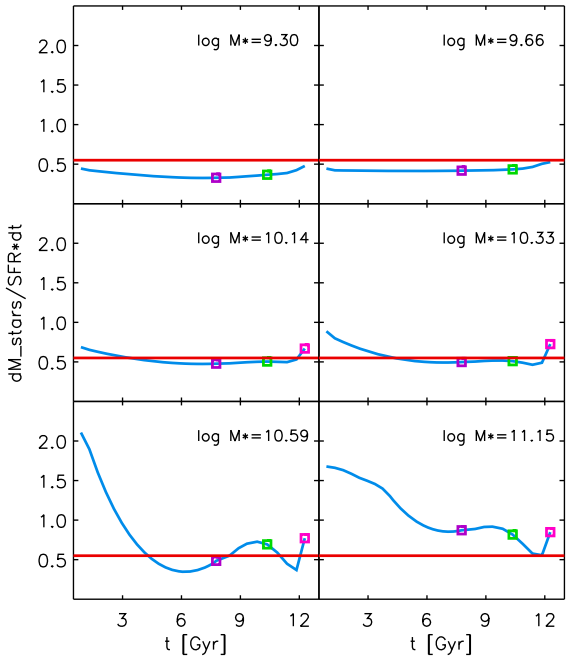

Figure 12. Changes of stellar mass in units of star formation as a function of lookback time for six galaxies with different final stellar mass. The red curves correspond to lookback model calculations. The blue curves are calculated from the Magneticum evolution sample. Violet, green and pink squares indicate redshifts z = 1, 2 and 4.2, respectively. For discussion, see text.

However, at this point we need to add a word of caution. We note that our method to calculate Magneticum accretion rates is based on the assumption that the increase of stellar mass is solely through star formation. If the increase of stellar mass is also partially caused by merging with infalling galaxies, then our approach underestimates the accretion rates and provides only lower limits.

6.4. *Stellar mass growth and merging*

In order to estimate the influence of merging on the growth of stellar mass we determine the ratio

$$\Lambda_* = \frac{\Delta M_*}{\psi \Delta t}. \tag{23}$$

For the lookback models we have the constant value Λ_* = 1 - R. This is the horizontal red line in Fig. 12. The blue curve shows the results obtained from the Magneticum evolution sample. We find good agreement with the simple lookback model approach for the mass bins log M = 10.16 and 10.34. This implies mass return fractions to the ISM during the star formation process of R ≈ 0.45, as we have adopted for the lookback models. For smaller masses the blue curves for the Magneticum models indicate somewhat larger return fractions of R ≈ 0.6 to 0.7. For the two highest mass bins there is a clear indication of merging at lookback times t $\lesssim$ 3 and 6, respectively, with Λ_*-values clearly larger than unity. As a consequence, the Magneticum accretion rates for these phases of the evolution of the Magneticum high mass models are likely larger than indicated in Fig. 11.

6.5. *Magneticum star forming gas masses, star formation time and the main sequence star formation law*

The Magneticum simulations provide the opportunity to investigate the connection between the main sequence star formation law ψ(z,M$_*$) and the gas mass - stellar mass relationship M$_g$(z,M$_*$). We do this in three steps. We first discuss the fraction of cold ISM gas, which is contributing to star formation. Second, we look at the time scale of the star formation process and, third, we combine this information with the predicted relation of total cold ISM gas mass (star forming and passive with respect to the star formation process) with stellar mass.

Not all the cold ISM gas in a galaxy is involved in the star forming process. In the Magneticum simulations only a fraction x$_g$

$$x_g(z(t), M_*) = \frac{M_g^{SF}(z, M_*)}{M_g(z, M_*)} \tag{24}$$

is producing stars. M$_g^{SF}$ is the total mass of all cold star forming ISM gas and correponds to gas of low temperature above a certain density threshold. Fig. 13 uses the Magneticum snap shot sample (restricted to galaxies with log $|\psi/\psi_{LB}| \leq 0.25$, the Magneticum main sequence) and the evolution sample to demonstrate how x$_g$ depends on redshift and stellar mass and how it evolves with lookback time t.

The snap shot sample plots show a significant scatter at lower redshift. However, observations of galaxies in the local universe show a similar scatter and the x$_g$ values observed agree with the Magneticum observations (see the XGASS, xCOLDGASS and MAGMA surveys, Saintonge et al. 2017, Catinella et al. 2018, Hunt et al. 2020).

The red curve is calculated with a fit formula (see Appendix B) to the Magneticum data, which closely matches the mean of x$_g$ as a function of stellar mass at each redshift. At low redshift x$_g$ is constant with stellar mass except at the lowest masses, where we find a strong increase. Towards higher redshift this behavior reverses: x$_g$ is constant at low masses, but declines towards higher masses. Most importantly, though, the maximum of x$_g$ increases with redshift. Unfortunately, there are no direct observations of HI available in galax-

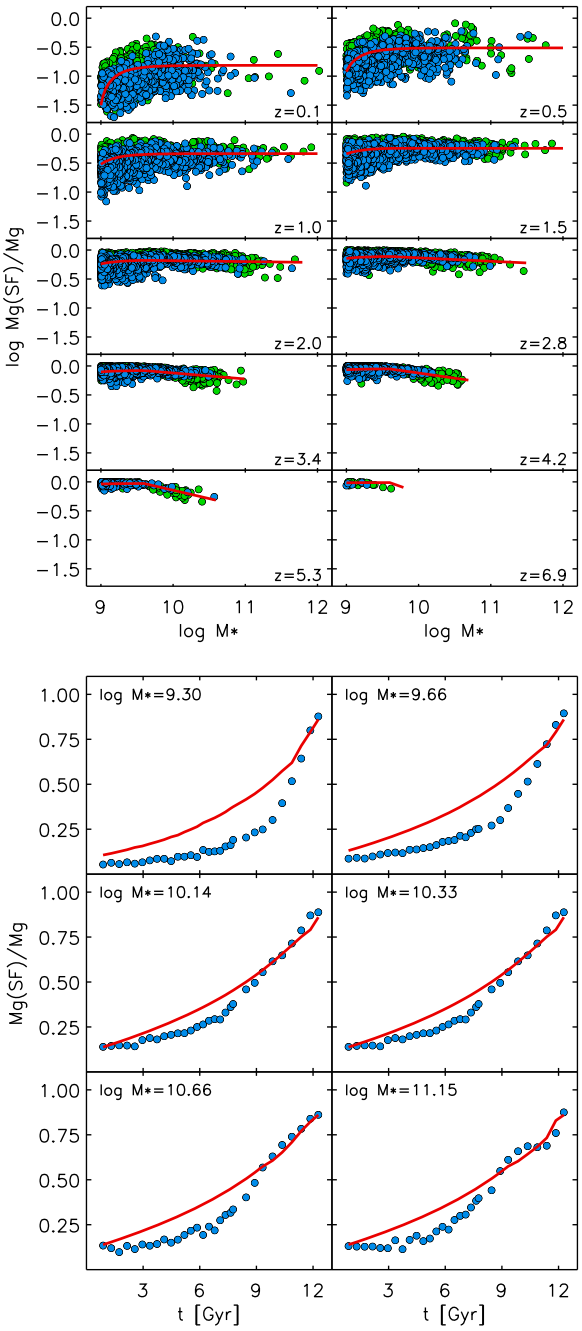

Figure 13. ISM fraction of the mass of star forming gas to total gas mass. Top: Magneticum snap shot sample at different redshifts with log $M_g(SF)/M_g$ as a function of stellar mass. Blue and green circles as before. Bottom: $M_g(SF)/M_g$ as a function of lookback time for the Magneticum evolution sample (blue circles) in six different stellar mass bins. The red curves correspond to the fit described in the text. A formula is given in Appendix B.

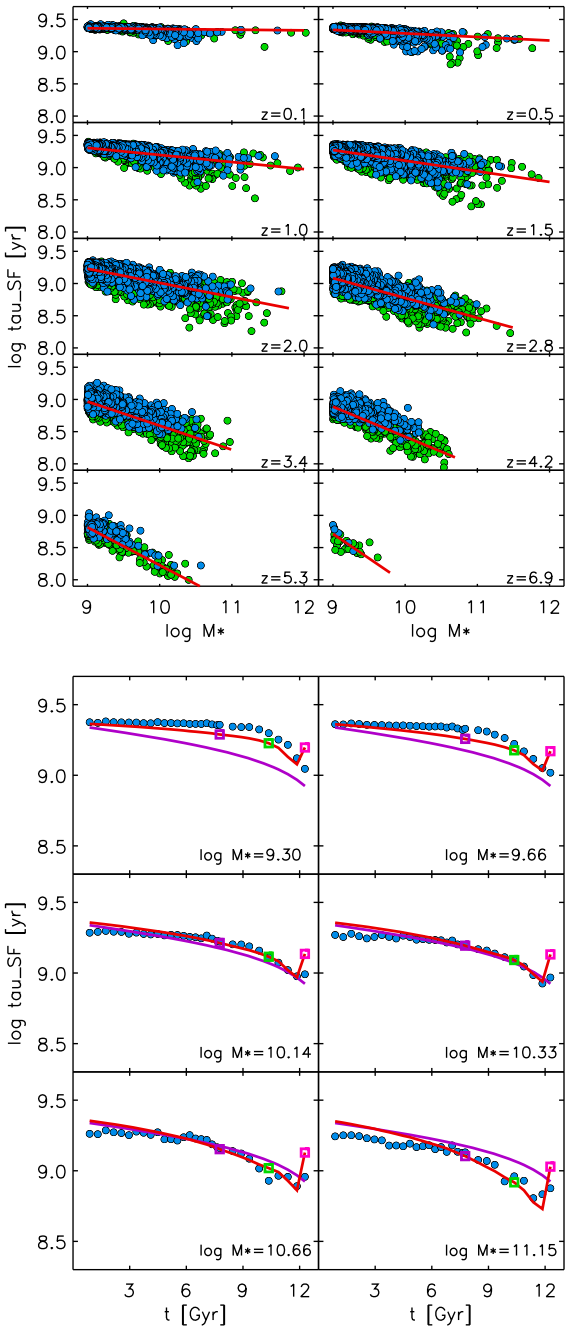

Figure 14. Logarithm of star formation time. Top: Magneticum snap shot sample at different redshifts with log τ_{SF} as a function of stellar mass. Blue and green circles as before. Bottom: τ_{SF} versus lookback time for the Magneticum evolution sample in six different stellar mass bins (blue circles). The red curves are calculated according to Appendix B and are discussed in the text. The violet curves are given by Eq. (26).

ies of higher redshift to compare with the Magneticum simulations.

The evolution sample plots demonstrate very clearly that during the course of the evolution of a galaxy x_g

decreases continuously. At the beginning of the life of a Magneticum star forming galaxy practically all gas is involved in the star formation process. But then the fraction of gas contributing to star formation becomes significantly smaller. The red curve is the fit taylored to describe the snap shot sample. While it is not a perfect fit for the evolution sample, it captures the evolution with time (and redshift) reasonably well.

We note that in observational studies - because of the lack of direct HI observations - the assumption is frequently made for the evolution of x_g that already at z $\approx$ 0.4 all cold ISM gas is involved in the star formation process, i.e. $xg \approx 1$ (see, for instance, Tacconi et al. 2018, 2020). The Magneticum simulations do not support this assumption. While a detailed comparison is beyond the scope of this paper, we note that other cosmological simulations (Lagos et al. 2015, Diemer et al. 2019, Davé et al. 2020) agree with Magneticum in this regard.

The timescale of the star formation process is given by

$$\tau_{SF}(z(t), M_*) = \frac{M_g^{SF}(z, M_*)}{\psi(z, M_*)}. \quad (25)$$

Fig. 14 shows τ_{SF} for the main sequence galaxies of the Magneticum snap shot sample and the evolution sample. The red line in the plots is a simple fit to the ridge line in the snap shot sample. The corresponding fit formula is given in Appendix B. We see that in the Magneticum galaxies the star formation time decreases with redshift. We also find a mass dependence with a negative slope, which becomes steeper with redshift. The Magneticum simulations at z $\sim$ 0.1 agree well with observations of galaxies in the local Universe (xGASS, xCOLDGASS, MAGMA). Observations at larger redshift (Tacconi et al. 2018, 2020) are also in agreement on average but they do not show the pronounced negative slope with stellar mass.

Comparing with a large sample of observed star forming galaxies Tacconi et al. (2018, 2020) suggest an empirical relationship of the form

$$\tau(t) = \tau_0(1 + z(t))^{-n}, \quad (26)$$

which we show in the plot of the Magneticum evolution sample in Fig. 14 using $\tau_0 = 2.3{\times}10^9$ yrs and n=0.6 (violet curve). We see that the Magneticum simulations have a similar trend as a function of lookback time (or redshift). The fit obtained from the Magneticum snap shot sample is in agreement with eq. (26). We note that our value for τ_0 is a factor of two larger than the one found by Tacconi et al. (2018). This is a consequence of the fact that the Magneticum SFRs are lower than the ones used by Tacconi et al. (2018) in the range of lookback time displayed here.

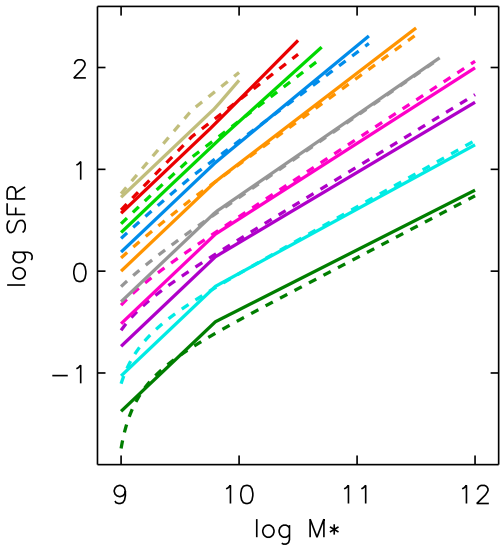

Figure 15. Lookback model SFRs ψ_{LB} as a function of stellar mass at the ten redshifts of the Magneticum snap shot sample from z = 0.1 to 6.9 (solid curves) together with SFRs calculated from eq. (27) (dashed).

With the fits for x_g and τ_{SF} as given in Appendix B we have an alternative way to calculate SFR as a function of redshift and stellar mass

$$\psi(z(t), M_*) = \frac{x_g^{fit}(z, M_*)}{\tau_{fit}(z, M_*)} M_g(z, M_*), \quad (27)$$

where M_g(z,M_*) is given by eq. (5). Fig. 15 compares lookback SFRs ψ_{LB} with SFRs calculated with eq. (27). We use the overall agreement found in Fig. 15 as an argument that the SFR law along the main sequence is a consequence of the power law relationship between total ISM gas mass and stellar mass. However, it is important to stress that the complex behavior as a function of redshift and stellar mass of xg, the ratio of star forming to total gas mass, and of τ_{SF}, the star formation timescale are also of crucial importance. Most importantly, we note that the decline of specific star formation rates (see Fig. 7) is not caused by the relatively small drop of the ratio M_g/M_* but rather by the significant continuous decrease of x_g(t). In other words, galaxies form less stars in the course of their evolution not because they are running out of gas (or because the star formation time changes dramatically) but rather because the fraction of cold ISM gas, which is capable of producing stars, becomes smaller.

6.6. *Chemical evolution*

One of the major goals of our lookback models has been to develop a tool to understand and interprete the chemical evolution of star forming galaxies. Here the key observation is the MZR between stellar metallicity and total stellar mass. Fig. 16 shows the V-band luminosity weighted average metallicity of the stellar population of the Magneticum snap shot sample as a function of stellar mass at different redshifts. The stellar metallicities of our lookback models calculated for two different effctive yields $[\mathrm{Z}]_0 = \log \frac{Y_N}{Z_\odot(1-R)} = 0.25$ (orange) and 0.35 (red) are also shown. There is a significant scatter of $\sigma_{[Z]} \approx 0.1$ to 0.15 dex in the Magneticum sample, but on average the lookback models reproduce the Magneticum MZRs reasonably well.

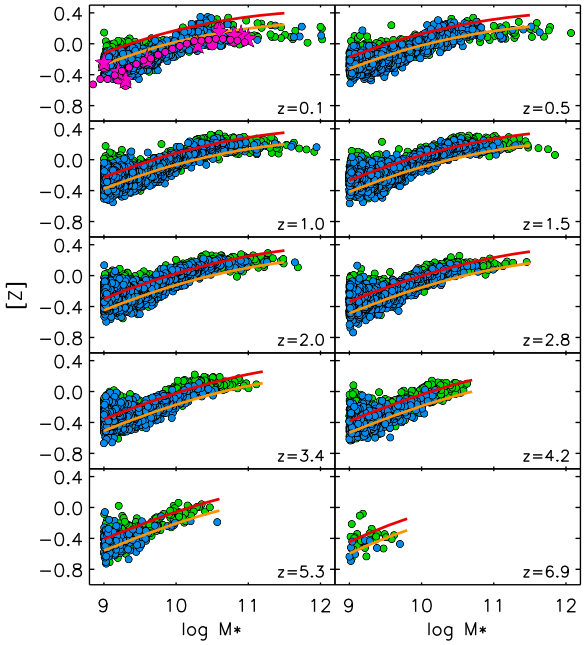

Figure 16. Luminosity V-band averaged stellar metallicities versus total stellar mass for the galaxies of the Magneticum snap shot sample at ten different redshifts. Lookback model stellar metallicities calculated for two different yields are overplotted in red and orange. At the lowest redshift observed stellar metallicities (see Fig. 2) are also shown as small and large pink circles and asterisks.

At the lowest redshift we also plot observed stellar metallicities which are systematically lower than Magneticum and which were fitted in section 3 with an effective yield lower by 0.15 and 0.25 dex, respectively. This systematic difference is slightly larger than the uncertainty of the observational stellar metallicity zero points which are about 0.1 dex (see references in section 3),

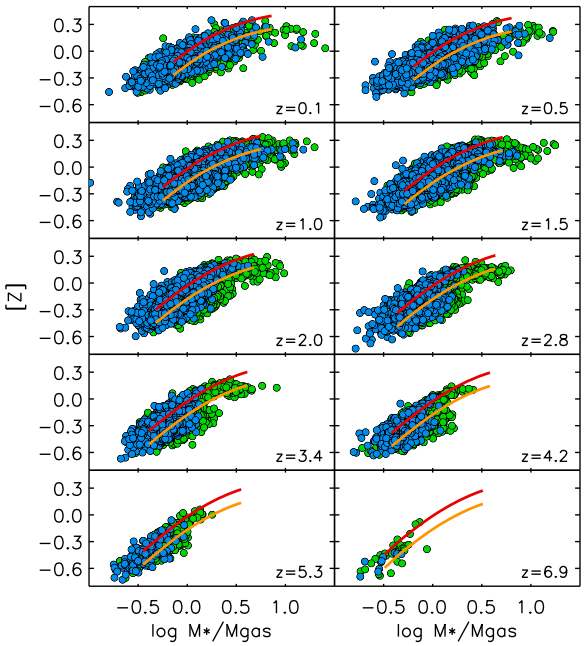

Figure 17. Stellar metallicities as a function of the ratio of stellar mass to total ISM gas mass. The galaxies of the Magneticum snap shot sample are compared with lookback model stellar metallicities again calculated for two different yields and overplotted in red and orange.

but can be addressed by changes of the yields in the simulations as demonstrated in Fig. 16.

An important consequence of the simplifying assumptions of our lookback models is the prediction that galactic metallicity is basically a function of the ratio of stellar mass to ISM gas mass. Fig. 17 confirms this conclusion by comparing lookback model stellar metallicities with Magneticum metallicities as a function of $\log \mathrm{M}_*/\mathrm{M}_g$.

The metallicity of the star forming ISM gas is expected to be slightly higher than the luminosity weighted metallicity of the stellar population, because the ISM metallicity represents the latest stage of the chemical evolution, whereas the stellar luminosity weighted metallicity always contains a contribution by the older population less advanced in the formation of heavy elements. Fig. 18 confirms this expectation. Note that we represent the metallicity of the star forming gas by its oxygen abundance relative to the sun $[\mathrm{O/H}]_{\mathrm{ISM}}$, which is usually determined from the observation of strong emission lines of the star forming gas. The difference $\Delta = [\mathrm{O/H}]_{\mathrm{ISM}}$ - [Z] is somewhat larger than the lookback models for most of the Magneticum galaxies but the effect is not large (0.1 to 0.15 dex) and disappears towards higher redshifts. We note that a small fraction of the Magneticum galaxies has negative values of Δ. We inter-

prete these as cases of recent accretion or merging with metal poorer gas involved.

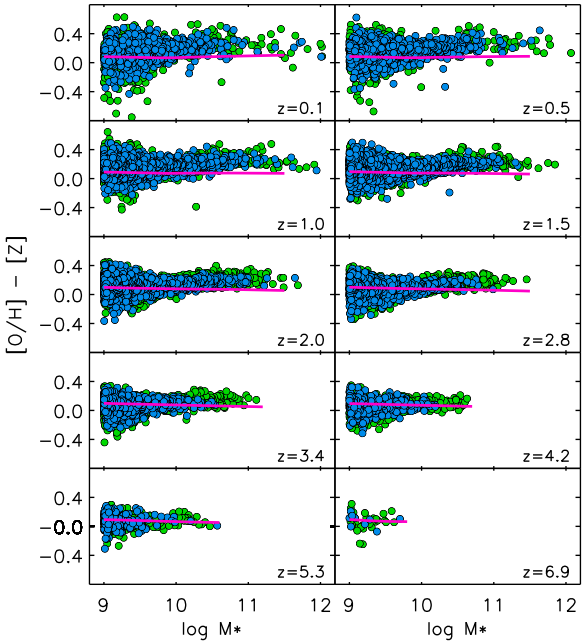

Figure 18. Difference between the oxygen abundance (relative to the sun) [O/H] of the star forming ISM gas and the luminosity weighted stellar metallicity [Z] (also relative to the sun) as a function of galaxy stellar mass. The galaxies of the Magneticum snap shot sample are plotted as circles in the usual way and the results obtained from the lookback model stellar metallicities are given by the pink line.

As was discovered by Mannucci et al. (2010) from a study of HII region emission lines, the MZR contains a dependence on a third parameter, the SFR. At fixed stellar mass, galaxies with lower SFR tend to have higher metallicities and vice versa. Z17 in their investigation of spectra of the integrated stellar population of 250000 SDSS galaxies found a similar effect for stellar metallicities. Most recently, Sanders et al. (2020) investigating galaxy gas-phase metallicities out to z $\sim$ 3.3, combined their SFRs and metallicities and, following the original work by Mannucci et al. (2010), presented a new fundamental relationship (FMR) between metallicity, stellar mass, star formation rate and redshift. In this framework, the evolution of the MZR with redshift is a consequence of the influence of SFR, which increases with redshift and leads to a decrease of metallicity. In addition, at a fixed redshift the range of SFRs encountered for galaxies at the same stellar mass contributes to the vertical width of the MZR with galaxies with lower SFRs having higher metallities and vice versa. We give an example in Fig. 19.

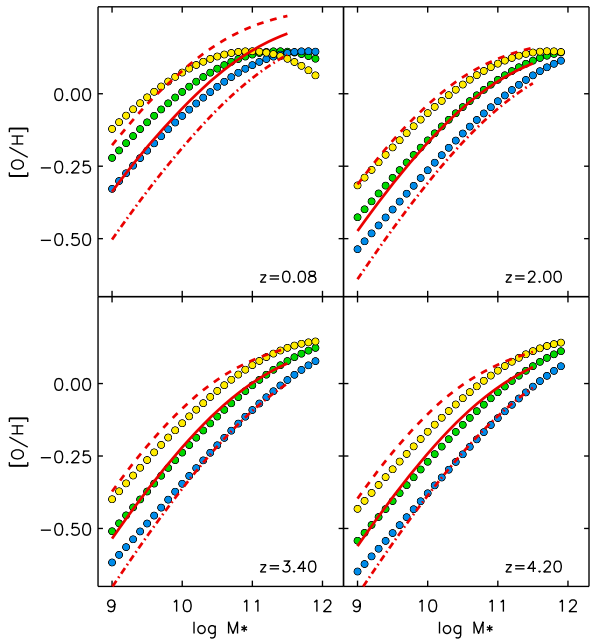

Figure 19. The observed effect of SFR on the MZRs at fixed redshift. Gas phase HII region oxygen abundances (relative to the sun) versus galaxy stellar mass are displayed at four redshifts. The circles correspond to observations and are obtained from the Sanders et al. (2020) FMR relationship adopting their SFR main sequence law (green) and systematic shifts away from the main sequence by $\pm$ 0.375 dex (yellow and blue, respectively). The red curves correspond to lookback model calculations on their main sequence (solid, see eq. 17 and Appendix B) and with the star formation shifts as described in the text (dashed and dashed-dotted).

In our lookback model approach metallicities do not depend directly on SFR. As explained in Appendix A, they depend foremost on M_*/M_g, the ratio of stellar to ISM gas mass and the evolution of the MZR with redshift is a result of the fact that the relation between gas and stellar mass is redshift dependent. Thus at first glance, the lookback models seem to be incapable in reproducing the observed SFR dependence of the MZRs at different redshift.

However, observations of galaxies in the local Universe show that the power law relationship between gas and stellar mass also depends on SFR. Galaxies with higher SFR have a higher ratio of gas mass to stellar mass and vice versa. Hunt et al. (2020) from the study of their MAGMA sample of galaxies find that the shift with SFR can be described by $\Delta\log Mg = x_\delta \Delta\log \psi$ with x_δ of the order of $\sim$ 0.4.

It is not surprising that such an additional SFR dependence exists. Galaxies with a higher (lower) gas mass at similar stellar mass and redshift will very likely also have an increased mass of the star forming cold ISM gas and, in consequnce, their SFRs will be higher (lower).

For our lookback models this has an important consequence. We obtain a SFR dependence of the MZR by assuming that galaxies with a systematic shift away from the lookback model main sequence by $\delta = \log \psi/\psi_{LB}$ have also a shift in the zero point of the gas mass stellar mass relationship by $\Delta\log A_0 = x_\delta\delta$ (see eq. 5 and 6 for the meaning of A_0). This is demonstrated in Fig. 19, where we compare our lookback models with the Sanders et al. (2020) MZRs calculated from their FMR formula. We adopt $\delta = \pm 0.375$ in this plot and $x_\delta = \pm 0.5$. In this way, the observed SFR dependence of the MZRs at fixed redshift is described reasonably well, as Fig. 19 indicates.

Fig. 20 shows again the crucial relationship between gas mass and stellar mass for the Magneticum snap shot galaxies, however this time we have introduced a color code with respect to the SFR. Galaxies with $\log \delta = |\psi/\psi_{LB}| \leq 0.20$ are plotted as green circles, galaxies with $\delta \geq 0.20$ in blue and galaxies with $\delta \leq 0.20$ in yellow. We see a clear offset of the blue and yellow circles relative to the green cicles in the overplotted background. This means that the Magneticum simulations also contain an SFR dependence in the relationship between gas mass and stellar mass. While we show only the highest redshifts of the snap shot sample, we note that the effect is also clearly present at lower redshift down to z = 0.5. Only at z = 0.1 the offset with SFR seems to disappear.

We also include the standard relationship for the lookback models in Fig. 20 and for two models with $\Delta\log A_0$ calculated with $\delta = \pm 0.375$ and $x_\delta = \pm 0.5$, respectively, as described above. We see that in this way the lookback models cover the SFR dependent range of gas masses encountered in the Magneticum simulations.

In Fig. 21 we display the SFR color coded Magneticum MZRs at the same four redshifts as in Fig. 20 together with the lookback models calculated with $\delta = 0, \pm 0.375$ and $x_\delta = 0, \pm 0.5$ in the same way as described for Fig. 20. The SFR dependence is clearly present in the Magneticum snap shot sample and the lookback models capture this effect well.

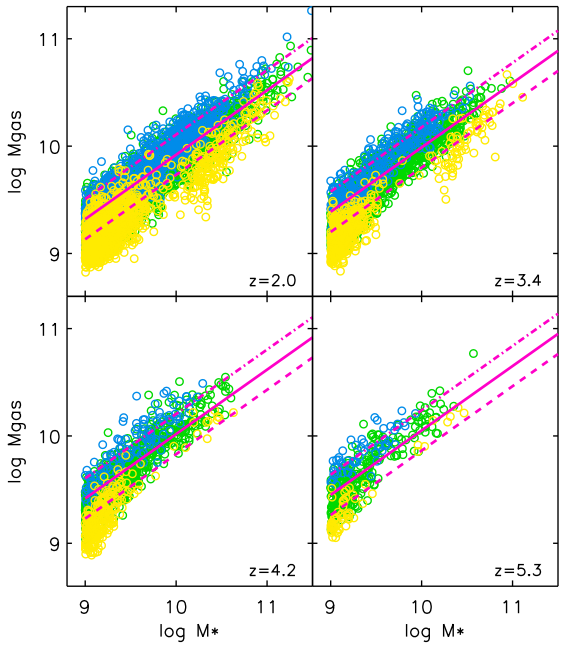

Figure 20. Magneticum galaxy gas mass versus stellar mass at four redshifts. The galaxies are color coded according to their SFRs. Green circles correspond to galaxies around the main sequence within 0.2 dex, yellow and blue circles are below and above the mains sequence, respectively. The pink solid line corresponds to the lookback model relation described by eq. 5 and 6, whereas the dashed and dashed-dotted lines use a shift of log A_0 in eq. 6 of this relation by $\pm$ 0.5·0.375. See text.

7. SUMMARY AND DISCUSSION

The main intention of the work presented here has been to develop lookback galaxy evolution models as a simple tool to describe galaxy formation and evolution, which can then be used to interprete observational results derived from spectroscopy such as the mass metallicity relationship or to calculate model spectra using population synthesis techniques. As a crucial test of this new tool we compare with the Magneticum cosmological simulations, which describe the process of galaxy formation and evolution in a much more comprehensive way.

An important ingredient for this comparison is the global galactic SFR as a function of stellar mass and redshift. A whole variety of such 'main sequence' relationships derived from observations is available in the literature and we have compared those with the Magneticum SFR. We found that the Magneticum SFRs are in the right ballpark but there is a systematic difference as a function of redshift. In order to use an SFR law for our lookback models that represents the Magneticum calculations well we have used the Pearson et al. (2018), Appendix C, relationship but with a correction factor as a function of redshift and with a modification of the power law, which describes the dependence of stellar mass.

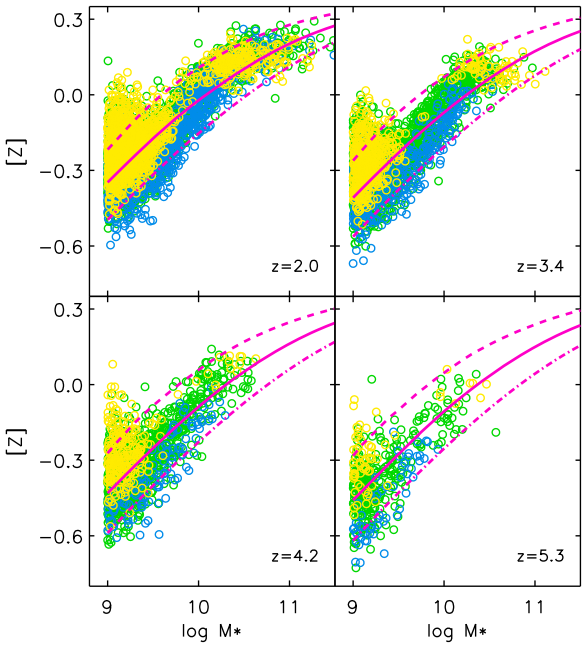

Figure 21. Stellar metallicities of Magneticum galaxies versus stellar mass at four redshifts. The galaxies are color coded according to their SFRs as in Fig. 20. The pink solid curve corresponds to lookback model calculations with the main sequence star formation law of eq. 17 and Appendix B adopted. The dashed and dashed-dotted curves apply shifts in SFR and in the gas mass stellar mass relation as described in the text.

In summary, we find that the lookback models capture many of the Magneticum galaxy properties reasonably well. Most importantly, their key assumption of a redshift dependent power law relationship between ISM gas mass and stellar mass agrees well with the Magneticum results. While a complex interplay of star formation, gas accretion and mass-loss by galactic winds obviously affects the galactic gas content, the net result, in a statiscal sense, is still that ISM gas mass is related to the stellar mass at all redshifts. This has important repercussions for the effective galactic gas accretion rates, which are larger than the rates of mass-loss through galactic winds but of the same order of magnitude as star formation rates.

The fraction of the cold star forming ISM gas to the total gas changes continuously with time in the Magneticum galaxies. At the early stage of galaxy formation all gas is involved in the star forming process but then during the further evolution with time the fraction of the gas contributing to star formation becomes significantly smaller. This is an important factor contributing to the main sequence star formation law. The specific star formation rates of star forming galaxies strongly decrease during the course of their evolution not because they are running out of gas (as described by the lookback model power law relationship between gas mass, redshift and stellar mass), but because the fraction of the still present cold ISM gas, which is capable of producing stars, becomes significantly smaller.

The luminosity weighted ages of the stellar population in the Magneticum galaxies are also described reasonably well by the lookback models. At low redshift there is a spread in ages, which can be explained by the spread in SFR, which we encounter in the Magneticum galaxies.

With the assumption of a redshift dependent relationship between ISM gas mass and stellar mass the lookback models predict that the average metallicity of a star forming galaxy depends on the ratio of stellar mass to ISM gas mass. Metal poor galaxies are gas rich and metal rich galaxies are gas poor. Indeed, the Magneticum galaxies follow this trend and the mass metallicity relationships at different redshifts of Magneticum and the lookback models are in good agreement. However, this requires an adjustment of the effective yield in the lookback models, for which the yield was originally calibrated so that observed MZRs in the local Universe obtained from spectroscopy of young stars or the integrated stellar populations agreed with the models. A comparison of Magneticum galaxies with these observations at low redshift shows a small offset in metallicity which is then covered by the adjustment of the effective yield.

The observed SFR rate dependence of the MZRs, which is also present in the Magneticum galaxies, can be reproduced by the lookback models in a very natural way. Galaxies with higher star formation rates are those with higher gas mass content, because they also have more star forming gas contributing to the star formation process. Therefore, their ratio of gas mass to stellar mass is higher and, as metallicity in the lookback models depends on the ratio of stellar to gas mass, their metallicity is lower.

The good agreement with the Magneticum simulations confirms that the lookback models provide a simple straightforward way to understand key aspects of the evolution of galaxies, such as the average gas accretion history, the star formation history and the formation of metals. This gives these models a great potential as tool for population synthesis calculations of synthetic spectra of the integrated stellar population of galaxies, which can then be used to constrain stellar metallicities from observed spectra. A typical example is given in the work by Zahid et al. (2017).

The advantage of the lookback models is that they are simple and easy to calculate. Their chemical evolution can be described by a simple analytical formula (see Appendix A) and a comparison with observations is straightforward. However, important aspects have not yet been covered in this first investigation. For instance, the chemical evolution describes only metallicity as a whole and does not distinguish between α- and iron group elements. The inspection of the Magneticum results shows that this approximation does not seem to lead to large errors, because the ratio of α over iron abundances does not change by more than 0.15 to 0.2 dex as a function of stellar mass or redshift, but it is a systematic and expected trend and it would be a clear improvement, if the models described this as well. We plan to implement this in future work in a way that still keeps the simplicity of these models.

This work has been supported by the Munich Excellence Cluster Origins funded by the Deutsche Forschungsgemeinschaft (DFG, German Research Foundation) under Germany's Excellence Strategy EXC-2094 390783311. The Magneticum Pathfinder simulations were performed at the Leibniz-Rechenzentrum with CPU time assigned to the Project "pr86re". We are especially grateful for the support by M. Petkova through the Computational Center for Particle and Astrophysics (C2PAP).

APPENDIX

A. ANALYTICAL SOLUTION OF THE METALLICITY EQUATION

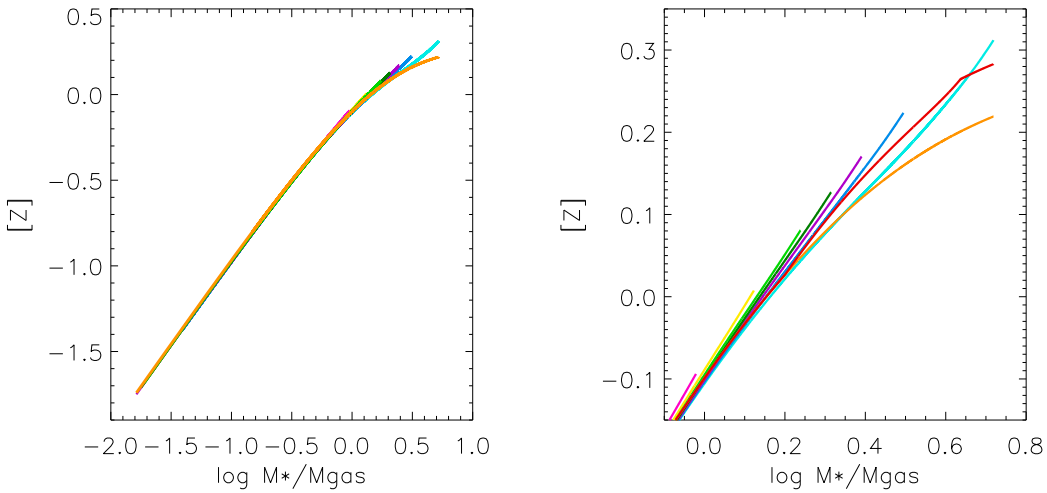

Figure 22. Top: Same as Fig. 1 but with the analytical solution of eq. (A6) overplotted in orange. Bottom: Enlarged plot of the upper right corner of the upper figure. The extended analytical solution of eq. (A8) is added in red.

Introducing the variable

$$x = \frac{1-R}{1-\beta(1-K)}\frac{M_*}{M_g} \tag{A1}$$

eq. (13) turns into

$$\frac{dZ}{dx} = \frac{Y_N}{1-R} - Z(1+\frac{\mu}{x}) \tag{A2}$$

with

$$\mu = \frac{\beta(1-K)}{1-\beta(1-K)}. \tag{A3}$$

The factor (1 - K) is roughly constant and close to unity for a large part of the evolution of a galaxy in our lookback model approach except at the lowest redshifts and the largest ratios of stellar to gas mass (log $M_*/M_g > 0.3$). It is straightforward to show that under these conditions

$$Z \approx Y_N \frac{1}{1+\mu} x (1 - \frac{1}{2+\mu} x), \quad \text{for } x \ll 1 \tag{A4}$$

or, alternatively,

$$Z \approx Y_N \frac{M_*}{M_g} (1 - \frac{1-R}{2-\beta(1-K)} \frac{M_*}{M_g}), \quad \text{for } x \ll 1. \tag{A5}$$

Eq. (A4) and (A5) explain - at least for small values of x - why the metallicity in our lookback models during the evolution of a galaxy depends mostly on the ratio of stellar mass to gas mass M_*/M_g.

The analytical solution of eq. (A2) for $\mu = 1$ is

$$Z = \frac{Y_N}{1-R} \frac{1}{x} (x - 1 + e^{-x}), \quad \text{for } \mu = 1. \tag{A6}$$

In Fig. 22 we overplot this analytical solution (assuming 1 - K = 0.85) to the individual numerical solutions of Fig. 1. We see that it is a good match to the numerical solutions except for large M_*/M_g, where it saturates and is ~ 0.1 dex too small. We also see that at these large values of stellar mass the individual numerical solutions do not lie exactly on top of each other but show a small dependence on the final mass at the lowest redshift. The reason is that towards large M_*/M_g values (corresponding to low redshifts) the factor (1 -K) starts to change and becomes very small and finally negative. This is caused by the increase of stellar mass and the fact the star formation rate ψ decreases towards lower redshifts (see eq. 12 for the definition of K). As a consequence, the term corresponding to dM_g/dM_* on the right hand side of eq. (13) becomes negative, which leads to an increase of Z rather than to a saturation. The slight divergence of the numerical solutions for different final stellar masses is the result of slightly different (1 - K) values in each model.

The behavior of K(M_*, z) at low redshift and large stellar masses also means that our analytical approximation using the variable transformation of eq. (A2) with (1 - K) = 0.85 breaks down. This contributes to the discrepancy encountered in Fig. 22. However, if we want to recover an analytical solution, we can introduce a correction term, which changes the metallicity saturation behavior for large mass ratios log $M_*/M_g \geqq 0.3$

$$c_Z(x) = \frac{1}{6} (\frac{\mu(x)}{x} - \frac{\mu(x_0)}{x_0}), \quad \text{for } x \geqq x_0 \tag{A7}$$

with x_0 the x-value at log $M_*/M_g = 0.3$. We limit c_Z(x) to a minimum value of -0.075 at the largest x-values. With this correction our new analytical solution is

$$Z = \frac{Y_N}{1 - R + c_Z(x)} \frac{1}{x} (x - 1 + e^{-x}), \quad \text{for } x \geqq x_0, \tag{A8}$$

which is shown in the enlarged plot on the right hand side of Fig. 22. In this plot we can again see how the individual numerical solutions for different final stellar masses diverge for log $M_*/M_g \gtrapprox 0.3$. As discussed above, the reason is the behavior of (1 - K) at large stellar masses, which is slightly different for each numerical solution. However, since this is a small effect, our main conclusion that in our look back models Z is a function of mainly M_*/M_g remains valid.

B. FORMULAE FOR ψ_{LB}, X_G^{FIT} AND τ_{FIT}

As described in section 5 we use the Pearson et al. (2018) SFR law of their Appendix C with several modifications. For the zero point we introduce the correction factor c(z) as described by eq. (17). In addition, we introduce a broken power law with respect to stellar mass

$$\psi_{LB} = \psi_0^{LB}(z) (M_*/10^{10.5})^{\delta(z)}, M_* \geq 10^{9.8}, \tag{B9}$$

$$\psi_{LB} = 0.2^{\delta(z)} \psi_0^{LB}(z) (M_*/10^{9.8})^{1.1}, M_* \leq 10^{9.8}. \tag{B10}$$

δ(z) and $\psi_0(z)$ are given in Pearson et al. (2018) in their Appendix C.

For redshifts z $\geq$ 3.42 we need to introduce an additional modfication to match the Magneticum SFRs at very low masses. We apply eq. (19) only in the range $10^9 \leq$M$_* \leq 10^{9.8}$. For lower masses we use

$$\psi_{LB} = 0.2^{\delta(z)} 0.132 \psi_0^{LB}(z)(M_*/10^9)^{\delta_l}, M_* \leq 10^9 \tag{B11}$$

with

$$\delta_l(z) = 1.1 - 0.6(1 - e^{(\frac{z-3.42}{0.4})^2}). \tag{B12}$$

The introduction of $\delta_l(z)$ leads to a transition of the power law exponent in this lower mass range from 1.1 to 0.5 when redshift increases. We find this trend in the low mass galaxies of the Magneticum evolution sample.

Our fit of star forming to total mass of the cold ISM gas, x_g^{fit} is calculated by

$$x_g^{fit} = 1 - a_g \cdot e^{-z/2} \tag{B13}$$

with

$$a_g(m) = 0.89 + 0.08 \cdot e^{4(m_{min}-m)}, m = \log M_*, m_{min} = 9.00 - 0.3(1 - e^{-5z}). \tag{B14}$$

The factor $e^{-z/2}$ shifts x_g^{fit} upwards with increasing redshift z, until it saturates at unity. The second term in a_g leads to a drop at low log M$_*$ and m_{min} regulates at which mass the drop sets in as function of z.

For z $\geq$ 1.5 and log M$_*$ $\geq$ 9.6 we need to account for the redshift dependent decline of x_g with stellar mass. We accomplish this by introducing Δz = z - 1.5 and using

$$x_g^{fit} = (1 - a_g(9.6) \cdot e^{-z/2}) 10^{-p(\Delta z)(m-9.6)}, z \geq 1.5, m \geq 9.6 \tag{B15}$$

with

$$p(\Delta z) = 0.02\Delta z(1 + 1.1\Delta z - 0.11\Delta z^2), a_g(9.6) = 0.89 + 0.08 \cdot e^{4(m_{min}-9.6)}. \tag{B16}$$

The Magneticum fit for the star formation time is

$$\log \tau_{fit} = a_\tau(z) - 0.11 \cdot z(m - 10.7), a_\tau = a_0(z) - 0.25 \cdot z \tag{B17}$$

with

$$a_0 = 9.15 + 0.22 \cdot w(z), w(z) = \frac{e^{-3(z-2.8)}}{1 + e^{-3(z-2.8)}}. \tag{B18}$$

The function w(z) causes a switch from $a_0 = 9.37$ at low z to $a_0 = 9.15$ at high z.

REFERENCES

Asplund, M., Grevesse, N., Sauval, A. J., & Scott, P. 2009, ARA&A, 47, 481, doi: 10.1146/annurev.astro.46.060407.145222

Behroozi, P. S., Wechsler, R. H., & Conroy, C. 2013, ApJ, 770, 57, doi: 10.1088/0004-637X/770/1/57

Bresolin, F., Kudritzki, R.-P., Urbaneja, M. A., et al. 2016, ApJ, 830, 64, doi: 10.3847/0004-637X/830/2/64

Catinella, B., Saintonge, A., Janowiecki, S., et al. 2018, MNRAS, 476, 875, doi: 10.1093/mnras/sty089

Chabrier, G. 2003, PASP, 115, 763, doi: 10.1086/376392

Davé, R., Crain, R. A., Stevens, A. R. H., et al. 2020, MNRAS, 497, 146, doi: 10.1093/mnras/staa1894

Diemer, B., Stevens, A. R. H., Lagos, C. d. P., et al. 2019, MNRAS, 487, 1529, doi: 10.1093/mnras/stz1323

Dolag, K., Mevius, E., & Remus, R.-S. 2017, Galaxies, 5, 35, doi: 10.3390/galaxies5030035

Elbaz, D., Daddi, E., Le Borgne, D., et al. 2007, A&A, 468, 33, doi: 10.1051/0004-6361:20077525

Genzel, R., Tacconi, L. J., Lutz, D., et al. 2015, ApJ, 800, 20, doi: 10.1088/0004-637X/800/1/20

Hirschmann, M., Dolag, K., Saro, A., et al. 2014, MNRAS, 442, 2304, doi: 10.1093/mnras/stu1023

Hunt, L. K., Tortora, C., Ginolfi, M., & Schneider, R. 2020, arXiv e-prints, arXiv:2010.02919. https://arxiv.org/abs/2010.02919

Kewley, L. J., & Ellison, S. L. 2008, ApJ, 681, 1183, doi: 10.1086/587500

Kobulnicky, H. A., & Kewley, L. J. 2004, ApJ, 617, 240, doi: 10.1086/425299

Komatsu, E., Smith, K. M., Dunkley, J., et al. 2011, ApJS, 192, 18, doi: 10.1088/0067-0049/192/2/18

Kudritzki, R. P., Castro, N., Urbaneja, M. A., et al. 2016, ApJ, 829, 70, doi: 10.3847/0004-637X/829/2/70

Kudritzki, R.-P., Ho, I.-T., Schruba, A., et al. 2015, MNRAS, 450, 342, doi: 10.1093/mnras/stv522

Lagos, C. d. P., Crain, R. A., Schaye, J., et al. 2015, MNRAS, 452, 3815, doi: 10.1093/mnras/stv1488

Lequeux, J., Peimbert, M., Rayo, J. F., Serrano, A., & Torres-Peimbert, S. 1979, A&A, 500, 145

Mannucci, F., Cresci, G., Maiolino, R., Marconi, A., & Gnerucci, A. 2010, MNRAS, 408, 2115, doi: 10.1111/j.1365-2966.2010.17291.x

Padovani, P., & Matteucci, F. 1993, ApJ, 416, 26, doi: 10.1086/173212

Pearson, W. J., Wang, L., Hurley, P. D., et al. 2018, A&A, 615, A146, doi: 10.1051/0004-6361/201832821

Peeples, M. S., Werk, J. K., Tumlinson, J., et al. 2014, ApJ, 786, 54, doi: 10.1088/0004-637X/786/1/54

Pettini, M., & Pagel, B. E. J. 2004, MNRAS, 348, L59, doi: 10.1111/j.1365-2966.2004.07591.x

Saintonge, A., Catinella, B., Tacconi, L. J., et al. 2017, ApJS, 233, 22, doi: 10.3847/1538-4365/aa97e0

Sanders, R. L., Shapley, A. E., Jones, T., et al. 2020, arXiv e-prints, arXiv:2009.07292. https://arxiv.org/abs/2009.07292

Schreiber, C., Pannella, M., Elbaz, D., et al. 2015, A&A, 575, A74, doi: 10.1051/0004-6361/201425017

Schulze, F., Remus, R.-S., Dolag, K., et al. 2018, MNRAS, 480, 4636, doi: 10.1093/mnras/sty2090

Speagle, J. S., Steinhardt, C. L., Capak, P. L., & Silverman, J. D. 2014, ApJS, 214, 15, doi: 10.1088/0067-0049/214/2/15

Springel, V., & Hernquist, L. 2003, MNRAS, 339, 289, doi: 10.1046/j.1365-8711.2003.06206.x

Tacconi, L. J., Genzel, R., & Sternberg, A. 2020, arXiv e-prints, arXiv:2003.06245. https://arxiv.org/abs/2003.06245

Tacconi, L. J., Genzel, R., Saintonge, A., et al. 2018, ApJ, 853, 179, doi: 10.3847/1538-4357/aaa4b4

Teklu, A. F., Remus, R.-S., Dolag, K., et al. 2015, ApJ, 812, 29, doi: 10.1088/0004-637X/812/1/29

Teklu, A. F., Remus, R.-S., Dolag, K., & Burkert, A. 2017, MNRAS, 472, 4769, doi: 10.1093/mnras/stx2303

Thielemann, F. K., Argast, D., Brachwitz, F., et al. 2003, in From Twilight to Highlight: The Physics of Supernovae, ed. W. Hillebrandt & B. Leibundgut, 331

Tremonti, C. A., Heckman, T. M., Kauffmann, G., et al. 2004, ApJ, 613, 898, doi: 10.1086/423264

van den Hoek, L. B., & Groenewegen, M. A. T. 1997, A&AS, 123, 305, doi: 10.1051/aas:1997162

Wiersma, R. P. C., Schaye, J., & Smith, B. D. 2009, MNRAS, 393, 99, doi: 10.1111/j.1365-2966.2008.14191.x

Woosley, S. E., & Weaver, T. A. 1995, ApJS, 101, 181, doi: 10.1086/192237

Zahid, H. J., Dima, G. I., Kewley, L. J., Erb, D. K., & Davé, R. 2012, ApJ, 757, 54, doi: 10.1088/0004-637X/757/1/54

Zahid, H. J., Dima, G. I., Kudritzki, R.-P., et al. 2014, ApJ, 791, 130, doi: 10.1088/0004-637X/791/2/130

Zahid, H. J., Kudritzki, R.-P., Conroy, C., Andrews, B., & Ho, I. T. 2017, ApJ, 847, 18, doi: 10.3847/1538-4357/aa88ae